Nanoscale Horizons

ROYAL SOCIETY OF CHEMISTRY

COMMUNICATION

View Article Online
View Journal | View Issue

Cite this: *Nanoscale Horiz.*, 2026, **11**, 525

Received 29th July 2025,
Accepted 27th November 2025

DOI: 10.1039/d5nh00540j

rsc.li/nanoscale-horizons

Chemically anchored metal–hydrogel bilayers for ultrasoft and metallic biointerfaces

Yoon A Lee, †[ab] Jun Yong Lee, †[ab] Jeeyoung Kim, [ab] Hyunjin Lee, [ab] Seonghae Park, [ab] Sung-Hyuk Sunwoo,*[c] Gi Doo Cha*[d] and Dae-Hyeong Kim *[ab]

Metals are essential components of bioelectronic systems, such as contact electrodes, interconnects, and sensors. However, their inherent rigidity poses major challenges for integration in soft bioelectronics. In particular, the mechanical mismatch between metals and biological tissues can cause reduced signal fidelity and unwanted tissue damage. To address these issues, various geometrical engineering approaches have been explored to increase the deformability of metals. For example, strain-relief layers have been investigated; however, physically laminated structures often fail to adequately dissipate strain under deformation. Here, we present a chemically conjugated, monolithic metal–hydrogel bilayer, imparting high deformability to metals with minimal compromise in electrical conductivity. The formation of chemically anchored ligand interactions between the metal and hydrogel induces uniform wrinkles in the metal layer, effectively mitigating stress concentration. Consequently, the monolithic bilayer exhibits ultrasoft mechanical properties and metallic electrical performance, including high electrical conductivity, low impedance, tissue adhesion, and stretchability. The chemical anchoring process is spatially programmable, making it suitable for the fabrication of arrays of soft bioelectronic devices. We validated the performance and functionality of this platform in cardiac applications, demonstrating its efficacy in both electrophysiological recording and electrical stimulation.

New concepts

This study introduces a ligand-mediated transfer technique to fabricate a metal–hydrogel bilayer for ultrasoft and highly conductive bio-interfaces. Through chemical anchoring of the PVA–PAA hydrogel with the deposited Au thin film through a transfer process, the transferred Au forms a wrinkled structure on the hydrogel surface. By dissipating mechanical strain, such morphology aids in retaining high conductivity under deformation. This allows the bilayer to maintain high signal fidelity in dynamic biological environments. The hydrogel contributes intrinsic softness to the system, facilitating mechanical compliance with soft tissues. Furthermore, in regions without metal coverage, the adhesive hydrogel directly contacts the tissue and forms covalent bonding, supporting conformal contact and stable fixation of the device. In short, the metal–hydrogel bilayer exhibits four key features: (1) high conductivity, (2) patternability, (3) tissue adhesiveness, and (4) mechanical softness, within a monolithic biointerface. This multifunctional design, combined with bioelectronics, holds strong potential for next-generation digital healthcare, where high-resolution and stable signal acquisition is required. The use of chemically anchored metal–hydrogel bilayers as functional biointerfaces is expected to establish a foundational milestone for future bioelectronics research.

1. Introduction

Metals, due to their excellent electrical conductivity, are indispensable in modern electronic systems.[1,2] They serve as conductors in electronic devices, carry electrical currents, interconnect device components, and detect biological signals.[3–5] In the field of bioelectronics, metals also play a crucial role,[6,7] but the mechanical mismatch between rigid electronics and soft biological tissues leads to non-conformal contact, elevated impedance, mechanical tissue damage, and severe inflammatory responses.[8–10]

To address these challenges, soft bioelectronics have emerged, aiming to achieve seamless integration between electronic devices and biological tissues by mitigating mechanical mismatch.[11–13] In this context, imparting softness[14] and stretchability[15] to metals has garnered considerable interest. Various geometric engineering strategies, such as using ultrathin metal films, designing serpentine patterns, and

[a] *Center for Nanoparticle Research, Institute for Basic Science (IBS), Seoul, 08826, Republic of Korea*
[b] *School of Chemical and Biological Engineering, Institute of Chemical Processes, Seoul National University, Seoul, 08826, Republic of Korea. E-mail: dkim98@snu.ac.kr*
[c] *Department of Chemical Engineering, Inha University, Incheon, 22212, Republic of Korea. E-mail: shsunwoo@inha.ac.kr*
[d] *Department of Systems Biotechnology, Chung-Ang University, Ansung, 17546, Republic of Korea. E-mail: cgidoo@cau.ac.kr*
† These authors contributed equally to this work.

inducing out-of-plane buckling, have been proposed to increase metal deformability.[16,17] However, geometric approaches remain fundamentally limited in overcoming the intrinsic stiffness of metals. On the other hand, soft conductive nanocomposites, that incorporate metallic nanomaterials within polymer networks, have also been explored.[18–20] Various kinds of nanocomposites have garnered considerable attention as soft conductors due to their inherent softness and considerable conductivity.[21–23] However, these nanocomposites typically exhibit inferior electrical conductivity and limited patternability compared to pure metals.

As an alternative strategy to enhance metal deformability, the use of soft substrates combined with deposited,[24–26] or transferred[27] thin metal films has also been explored. Elastomers are widely employed as substrates in soft electronics due to their effective stress-absorbing properties and ease of processing.[28–32] However, their Young's moduli, typically in the MPa range, significantly exceed those of soft biological tissues.[33] In contrast, hydrogels exhibit tissue-like architectures with extremely low Young's moduli in the kPa range. Despite their tissue-like softness, it remains challenging to maintain their inherent softness throughout the metal deposition process. Moreover, physical lamination of metal films onto hydrogel substrates often results in weak interfacial adhesion,[34–36] leading to interfacial slippage under mechanical deformations, mechanical instability, degraded electrical performance, and eventual device failure.

Here, we present a metal–hydrogel bilayer electrode by transferring a thin gold film onto a soft hydrogel substrate through a ligand-mediated transfer strategy. This material design integrates the intrinsically high electrical conductivity of the metal with the ultrasoft mechanical property of the hydrogel. The transfer process of the metal layer onto the soft hydrogel surface, which accompanies chemical anchoring between bilayers, exhibits high yield and reproducibility regardless of the pattern geometry. Furthermore, by using adhesive hydrogels, the conformal and stable integration of the device with various tissues is allowed. These advantages, including mechanical compliance, robust adhesion, reliable electrical performance and versatile patternability, comprehensively contribute to the chemically anchored bilayer for overcoming the limitations of previous bioelectrode materials. The potential of this bilayer as a soft biointerface was successfully demonstrated in a rodent cardiac model under dynamic conditions.

Dae-Hyeong Kim

Dae-Hyeong Kim is a Professor of Chemical and Biological Engineering at Seoul National University and an Associate Director of the IBS Center for Nanoparticle Research. His research focuses on nanomaterial-based soft and biointegrated electronics. Over the past decade, he has built a meaningful relationship with Nanoscale Horizons, contributing works on electronic skin and stretchable electroluminescent devices. He is pleased to join the 10th anniversary collection with recent advances in soft electrodes and congratulates the journal on its continued leadership in nanoscale science.

2. Results and discussion

2.1. Metal–hydrogel bilayer for a soft, conductive biointerface

The metal–hydrogel bilayer was fabricated using a ligand-mediated transfer technique that enables the direct integration of patterned Au thin films onto adhesive (poly(vinyl alcohol)/poly(acrylic acid)) (PVA–PAA) hydrogels (Fig. 1(a), left). Conventional vacuum-based metal deposition onto hydrogels leads to dehydration and stiffening of the hydrogel (Fig. 1(b), inset), thereby compromising its mechanical integrity and deteriorating intrinsic performance of the deposited metal (Fig. S1 and S2).[37] In contrast, our ligand-mediated transfer method for the metal–hydrogel bilayer preserves both the inherent softness of the hydrogel and the electrical conductivity of the metal (Fig. 1(b)).[21,38–44] The simultaneous implementation of these features, such as high electrical conductivity and tissue-like softness, without compromising their performance, is a key advantage of this work in contrast to previous studies.

The key mechanism of this method relies on specific chemical interactions at the metal–hydrogel interface (Fig. 1(a), right). A self-assembled monolayer of 6-amino-1-hexanethiol is first grafted onto the Au film surface. Subsequently, a PVA–PAA hydrogel precursor solution containing acrylic acid *N*-hydroxysuccinimide ester (AA–NHS) is cast onto the ligand-functionalized Au surface. Upon ultraviolet irradiation, covalent bonds form between PVA–PAA hydrogel and 6-amino-1-hexanethiol, and the hydrogel undergoes crosslinking for gelation. After curing, the resulting metal–hydrogel bilayer is delaminated from the handling substrate, during which a wrinkled metal morphology is induced.

The metal–hydrogel bilayer features covalent bonding at the interface, ensuring robust adhesion and reliable transfer of the thin metal film onto the ultrasoft hydrogel substrate. This mechanical robustness enables preserving electrical performance under mechanical deformation. For example, a light-emitting diode integrated with a mesh-patterned metal–hydrogel bilayer remained illuminated under uniaxial strain (Fig. 1(c)). Cross-sectional imaging confirmed a seamless interface between the metal and hydrogel layers, confirming successful integration (Fig. 1(d)). To demonstrate the potential applicability of this platform, we fabricated an epicardial patch based on the metal–hydrogel bilayer (Fig. 1(e)), highlighting its promise as a stretchable, conductive, and patternable biointerface.

2.2. Design strategies for metal–hydrogel bilayers

During the chemical anchoring process between the metal and the hydrogel, the thiol group of the ligand formed strong Au–S

bonds with the Au thin film,[45] while the terminal amine group reacted with the AA–NHS group in the hydrogel matrix to form covalent amide linkages (Fig. 2(a)).[46] Fourier-transform infrared spectroscopy (FT-IR) was performed to identify the formation of amide bonds between 6-amino-1-hexanethiol and AA–NHS (Fig. 2(b)). The FT-IR spectra showed characteristic peaks to amide carbonyl (C═O) and amine (C–N) bonds at approximately 1700 (amide I) and 1450 cm^{-1} (amide II),

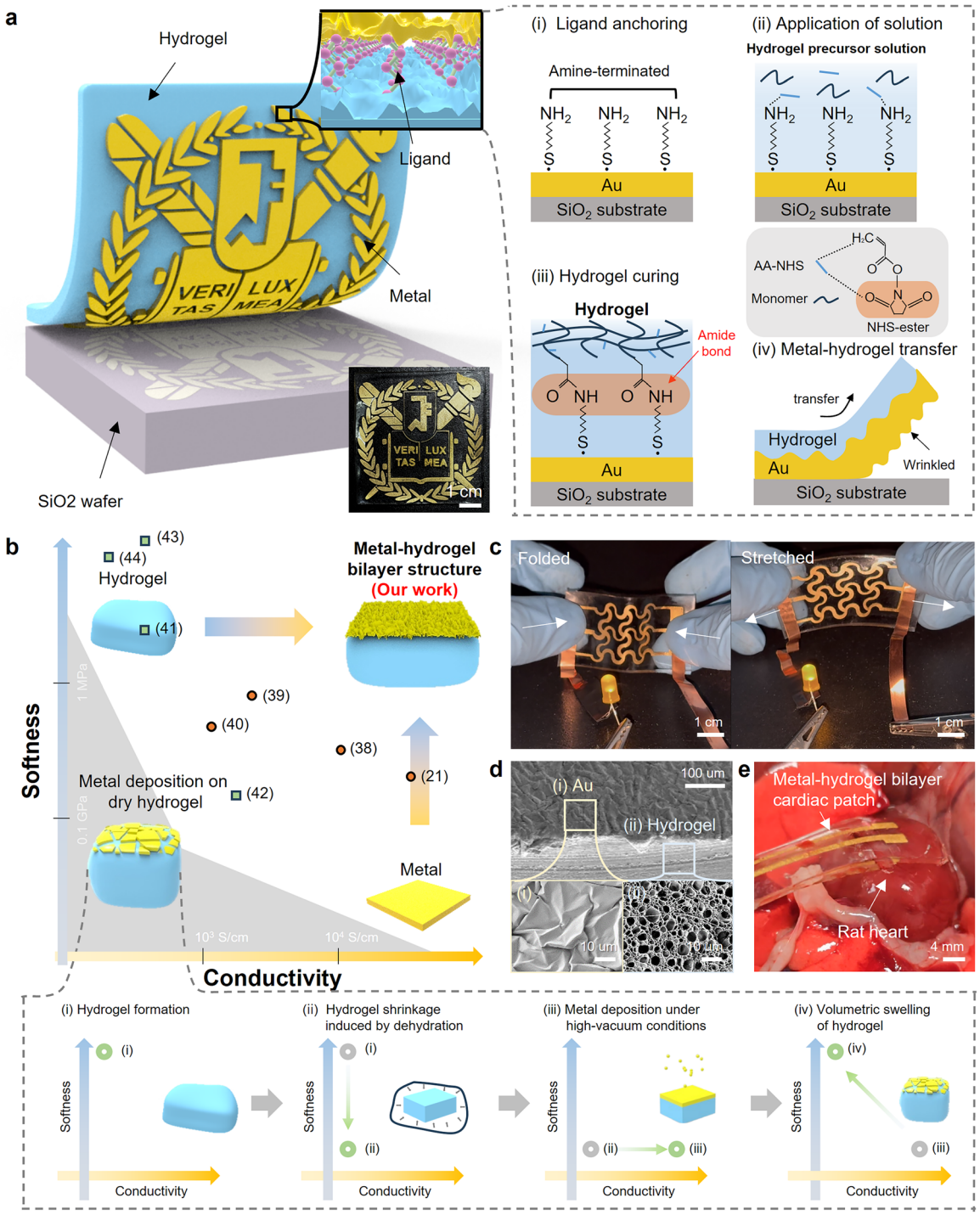

Fig. 1 Ligand-assisted transfer printing of metal onto hydrogel and its application to soft bioelectronics. (a) Schematic illustration of the ligand-assisted metal transfer printing process (left) and its chemistry (right). (b) Comparative positioning of the metal–hydrogel bilayer on the electrical conductivity *versus* softness and (inset) the comparison with metal deposited on the dry hydrogel. Square symbols represent hydrogel-based composites (ref. 41–44), while circle symbols denote elastomer-based composites (ref. 21 and 38–40) reported in previous studies employing metallic fillers. (c) Optical photograph of an LED-integrated metal–hydrogel bilayer under mechanical deformation. (d) SEM images of the metal–hydrogel bilayer. (e) Optical photograph of the metal–hydrogel bilayer conformally laminated onto a rat heart.

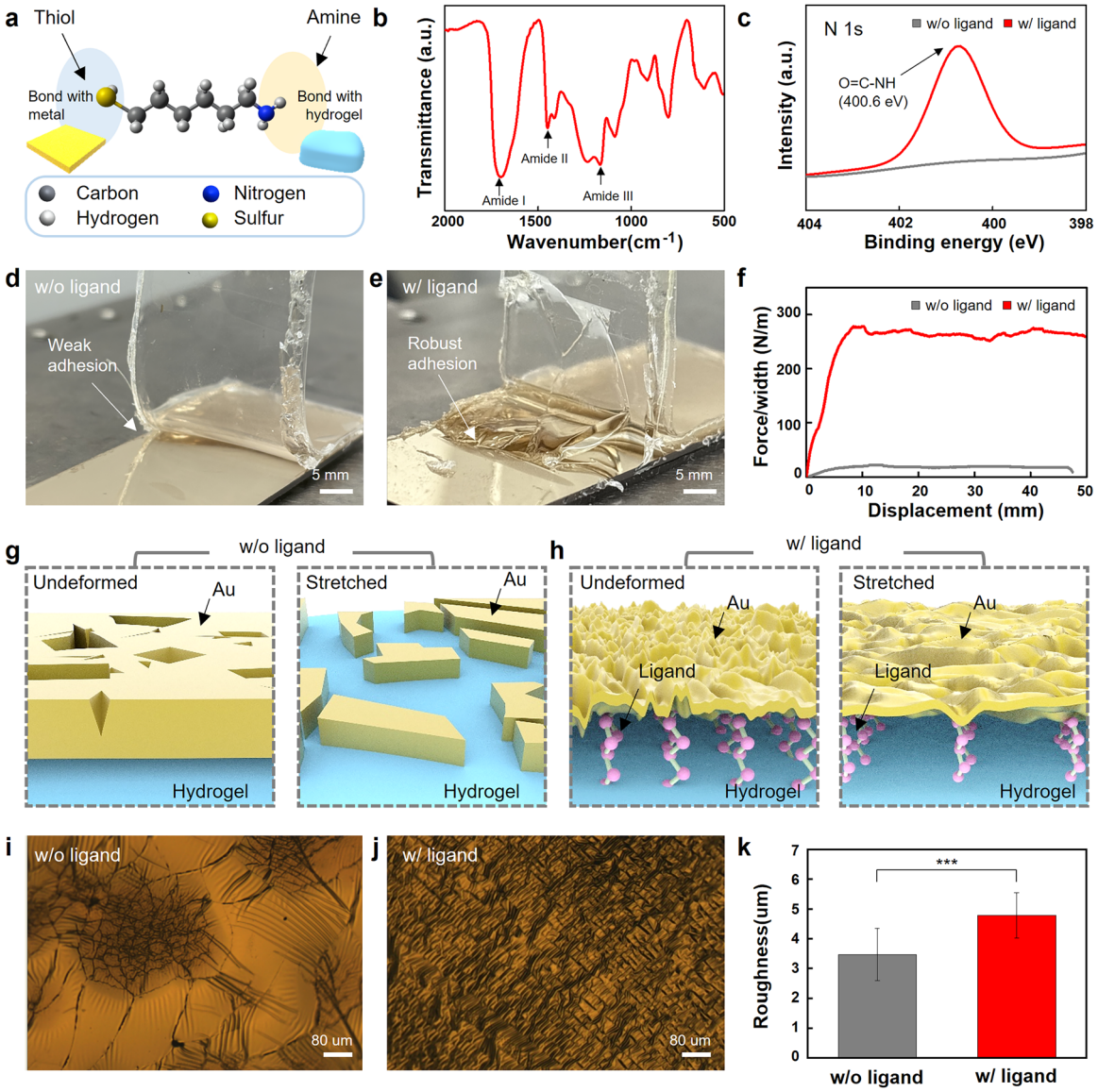

Fig. 2 Strong interfacial bonding between metal and hydrogel through ligand conjugation. (a) Schematic illustration of 6-amino-1-hexanethiol, highlighting the functional groups involved in chemical bonding between Au and hydrogel. (b) FT-IR spectra showing amide bond formation between chemically anchored Au and PVA–PAA hydrogel. (c) XPS analysis demonstrating the presence of amide peaks, supporting chemical linkage at the Au-hydrogel interface. (d) and (e) Optical photographs of 90-degree peel tests showing poor adhesion with the physically laminated hydrogel (left) and robust interfacial bonding with a chemically anchored hydrogel (right). (f) Curves of the peeling force per width *versus* displacement. (g) and (h) Schematic illustration of the surface morphology of the Au film before and after the stretching process. (i) and (j) Optical images of the Au surface showing the presence of ligands affects the morphology of the Au film after the transfer process. (k) Quantitative comparison of roughness between physically laminated (grey) and chemically anchored (red) Au films (n = 20, each).

respectively.[47] X-ray photoelectron spectroscopy further confirmed the formation of amide bonds (Fig. 2(c)).[48] The nitrogen (N 1s) peak in the ligand–anchored hydrogels was observed (400.6 eV), compared to the sample without ligand anchoring, indicating successful covalent bonding between the hydrogel and Au thin film. The mechanical integrity of the bilayer was assessed by performing 90° peel tests to quantify the interfacial toughness. The ligand-mediated interface demonstrated strong adhesion, as evidenced by partial hydrogel failure during peeling and the residual hydrogel remaining on the Au surface (Fig. 2(e)). In contrast, the samples with physically laminated hydrogel on the Au surface exhibited clear delamination, showing poor interfacial adhesion (Fig. 2(d)). The interfacial toughness of the chemically integrated bilayer was $\sim$278 J m^{-2}, approximately 13 times higher than that of the physically attached interface ($\sim$20 J m^{-2}, Fig. 2(f)). These results highlight the efficacy of ligand-mediated chemical bonding in forming a robust and mechanically reliable metal–hydrogel interface.

The high interfacial toughness and mechanical adaptability of the chemical bilayer mainly contribute to the wrinkled microstructure formation during the transfer process. In physically laminated bilayers without ligand conjugation, the metal

film is flatly formed and easily fractured under strain (Fig. 2(g)). In addition, the transfer yield of the metal onto the hydrogel decreases due to the low interaction force between materials. By contrast, the chemically anchored bilayers maintain their structural integrity and electrical continuity even under mechanical deformation (Fig. 2(h)), because the wrinkled microstructure effectively dissipates the strain.[26,49,50]

The microstructures of the physically laminated bilayer and the chemically anchored bilayer were observed using optical microscopic images. Without chemical anchoring, the distribution of the wrinkled structure is heterogeneous, implying that the applied strain will be localized on specific regions (Fig. 2(i)). This would cause the metal network to break easily. In contrast, the microstructure of the chemically conjugated bilayer exhibits a homogeneous wrinkled morphology (Fig. 2(j)), which indicates that such structure could effectively delocalize the applied strain. Quantitative analysis revealed that the roughness of the chemically integrated bilayer is higher than the physically laminated bilayer (Fig. 2(k)). These differences in morphology are expected to enhance the electrical stretchability of the bilayer by maintaining the conductive pathways under deformation.[26]

2.3. Material characterization of the bilayer

The metal side of the bilayer is in direct contact with the target tissue, which facilitates electrical signal transduction between the device and the tissue. Electrical performance should remain stable under external strain, such as that caused by tissue deformation. Chemical anchoring between the metal and the hydrogel guarantees stable electrical performance up to ~50% strain (Fig. 3(a)), which is superior to that of physically laminated bilayers (~10% strain), even surpassing the natural strain of the heart. Confocal microscopy images (Fig. 3(b)) showed that the wrinkled structure of the bilayer facilitates effective stress relaxation under stretching conditions, thereby enhancing its mechanical adaptability. Repetitive cycling tests demonstrated that the chemically anchored bilayer maintained durable electrical performance, whereas the physically

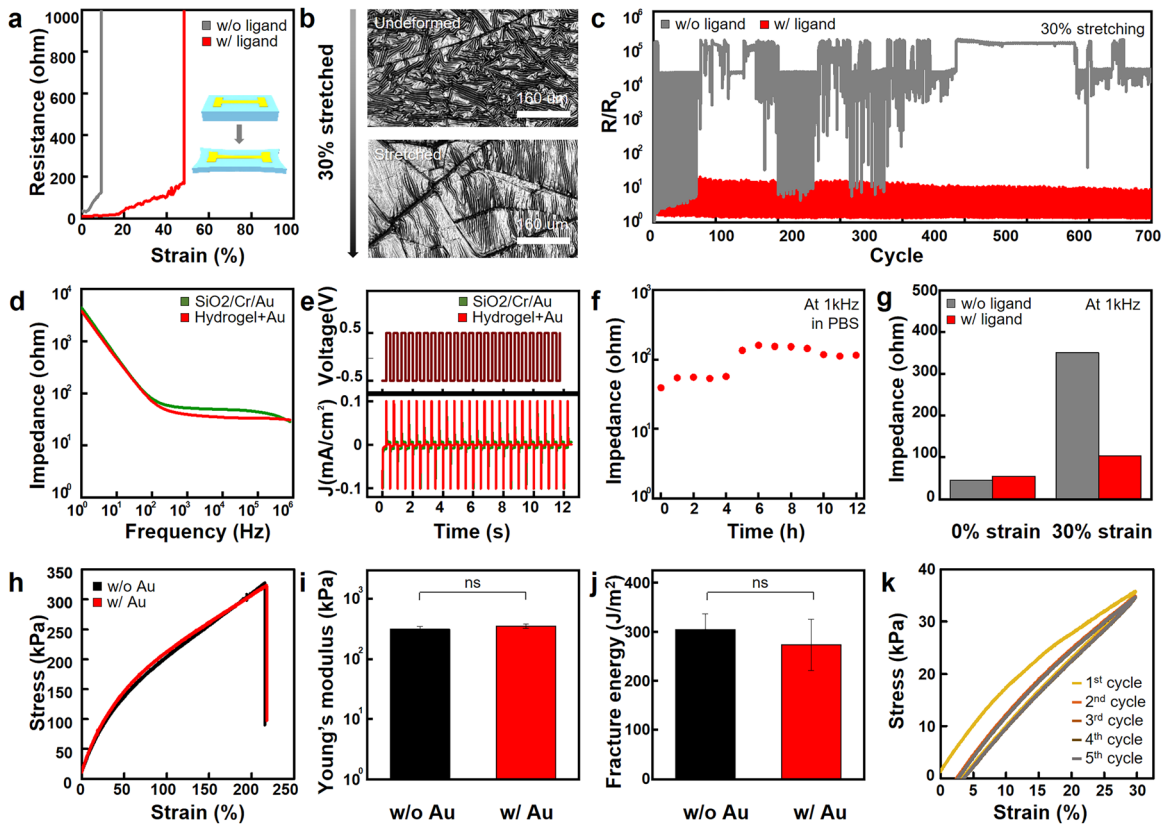

Fig. 3 Electrical, electrochemical, and mechanical properties of the metal–hydrogel bilayer. (a) Resistance changes under uniaxial strain for chemically anchored (red) and physically laminated (grey) samples. (b) Confocal microscopy scan image of the metal–hydrogel bilayer at 0% strain (top) and 30% strain (bottom). (c) Relative resistance change (R/R_0; R_0: initial resistance, R: instantaneous resistance) of the metal–hydrogel bilayer structure under cyclic strain between 0% and 30%. Comparison between chemically anchored (red) and a physically laminated (grey) bilayer. (d) Electrochemical impedance spectroscopy (EIS) of the metal–hydrogel bilayer (red) compared to Au on the SiO_2 substrate (green). (e) Current density of the metal–hydrogel bilayer (red) and Au on the SiO_2 substrate (green) as a function of applied voltage pulses. (f) Time-resolved impedance profile of the metal–hydrogel bilayer immersed in PBS solution. (g) EIS comparison of metal–hydrogel bilayers subjected to different ligand treatments and tensile strain levels. (h) Stress–strain curve of pristine hydrogel (black) and Au-transferred hydrogel (red). (i) Young's modulus of pristine hydrogel (black) and Au-transferred hydrogel (red) (n = 3, each). (j) Fracture energy of pristine hydrogel (black) and Au-transferred hydrogel (red) (n = 3, each). (k) Cyclic tensile stress–strain curve of the Au-transferred hydrogel under 30% strain.

laminated counterpart showed unstable degraded resistance (Fig. 3(c)). The bilayer also exhibited a slight increase in resistance, ensuring its long-term stability under *in vitro* conditions when integrated into the device configuration (Fig. S3). This stability further supports its potential for reliable integration with dynamic tissues such as the heart.

The fabrication of the bilayer did not compromise the electrochemical performance of the metal. When Au thin film was transferred onto the hydrogel, it exhibited impedance spectra like that of an ultrathin Au layer deposited onto the SiO_2 wafer (with a Cr adhesion layer) across all frequency ranges (Fig. 3(d)). In addition, the charge injection density of the bilayer was also compared with that of an Au thin film under the same voltage (Fig. 3(e)), corroborating that the electrochemical characteristics of the metal are not affected by chemical anchoring between the metal and the hydrogel. The impedance level rarely changed, even after soaking the bilayer in a phosphate buffered saline (PBS) solution for 12 h. This indicated that it had good electrochemical stability, necessary for *in vivo* applications (Fig. 3(f)). Electrochemical performance, including both charge storage capacity (CSC) and charge injection capacity (CIC), was similar in both cases of the chemically anchored and physically laminated bilayers (Fig. S4), demonstrating that the negligible variations in the initial electrochemical properties were observed between two bonding strategies before deformation. However, when subjected to 30% strain, the impedance of the chemically anchored bilayer changed only slightly, whereas the impedance of a physically laminated bilayer increased significantly (Fig. 3(g)). This result indicates that the wrinkled structure is essential for preserving electrochemical integrity under deformation. Chemical conjugation of the metal and the hydrogel forms a monolithic bilayer, without affecting the mechanical properties of the hydrogel. Only minor differences between the stress–strain curves (Fig. 3(h)) and Young's modulus (Fig. 3(i)) of the bare PVA–PAA hydrogel and the bilayer were observed. The fracture energies of both groups are also similar, demonstrating that the bilayer had excellent mechanical resilience against external deformation (Fig. 3(j)). No significant changes in the cycling stress–strain curves were observed, confirming the long-term mechanical durability of the bilayer (Fig. 3(k)). These results indicate that integrating a thin metal layer onto the hydrogel does not compromise the hydrogel's inherent soft mechanical nature, regardless of whether the layer is chemically anchored or physically laminated (Fig. S5).

The PVA–PAA hydrogel exhibits tissue-adhesive properties due to multiple interactions, including hydrogen bonding, covalent bonding, and polymer chain entanglement with biological molecules (Fig. 4(a)).[38,51] To be specific, the hydroxyl groups of the PVA chain and carboxylic acid groups of the PAA chain form hydrogen bonding with the primary amine groups on the tissue surface. Simultaneously, AA–NHS groups in the PVA–PAA hydrogel react with the primary amine groups on the tissue interface, forming covalent bonds at the hydrogel–tissue interface. Based on these multiple interactions, the metal–hydrogel bilayer could achieve conformal and stable adhesion to various tissue surfaces.

The hydrogel achieved conformal adhesion to abdominal muscle tissue without pre-treatment (Fig. 4(b)). Furthermore, it demonstrated exceptionally strong adhesion, as evidenced by the mechanical failure of the hydrogel rather than its detachment from the tissue. To quantitatively assess this adhesion performance, a lap-shear test was conducted on porcine skin (Fig. 4(c)) to compare the adhesive strength of the patterned metal–hydrogel bilayer with that of the hydrogel alone. The results showed comparable adhesion strengths (Fig. 4(d)), indicating that the integration of a hydrogel exposed part of the metal–hydrogel layer efficiently imparts the adhesion with the porcine skin. Moreover, the lap-shear tests performed on additional tissues, including liver, muscle and heart tissue *ex vivo* (Fig. S6), demonstrated that the metal–hydrogel bilayer maintains substantial adhesion across various types. The firm attachment of the bilayer to the tissue was further verified using a porcine heart *ex vivo* (Fig. 4(e)), which indicates that the bilayer can remain securely fixed even under dynamic conditions.

2.4. Fabrication of a patterned bilayer for *in vivo* applications

To implement the bioelectronics by using the bilayer, several layers are additionally fabricated for seamless integration (Fig. 5(a)). Anisotropic conductive film (ACF) is prepared for electrical connection with energy sources. The PVA–PAA hydrogel layer is once more synthesized with removal of the electrode region of the metal, for electrical insulation of the metal by exposure to untargeted tissues. The polydimethylsiloxane (PDMS) elastomer layer is prepared to prevent undesired adhesion to other organs, such as lungs and livers.

The fabrication process of bioelectronics using the bilayer is illustrated in Fig. 5(b). (i) First, the PVA–PAA hydrogel precursor solution was cured on top of a PDMS elastomer substrate. The elastomer substrate prevents undesired adhesion between the device and off-target organs. (ii) Second, thermally deposited Au was transferred onto the PVA–PAA hydrogel to form the bilayer. (iii) Third, the pre-formed PVA–PAA hydrogel was used to enhance tissue adhesion and prevent electrical leakage. These three layers, fabricated in parallel, were spatially aligned and assembled to implement the final bioelectronic device.

Chemical anchoring between the metal and the hydrogel polymer network also enhances the yield of the transfer process. The transfer yield of physically laminated bilayers (Fig. 5(c), top) and chemically anchored metal–hydrogel bilayers (Fig. 5(c), bottom) were investigated through different geometry of the metal film. The ligand-treated Au layer exhibited a high transfer yield, successfully transferred from the substrate to the target hydrogel, whereas the ligand-free Au layer showed markedly reduced transfer efficiency. This protocol can also be used to fabricate geometrically complex patterns with high resolution (Fig. 5(d)). Curvilinear patterning (serpentine pattern; Fig. 5(e)) was performed to evaluate the patterning resolution. An optically magnified image (Fig. 5(f)) shows well-defined pattern formation without errors, suggesting that the transfer process is compatible with high resolution patterning, which is highly advantageous for bioelectronics applications.

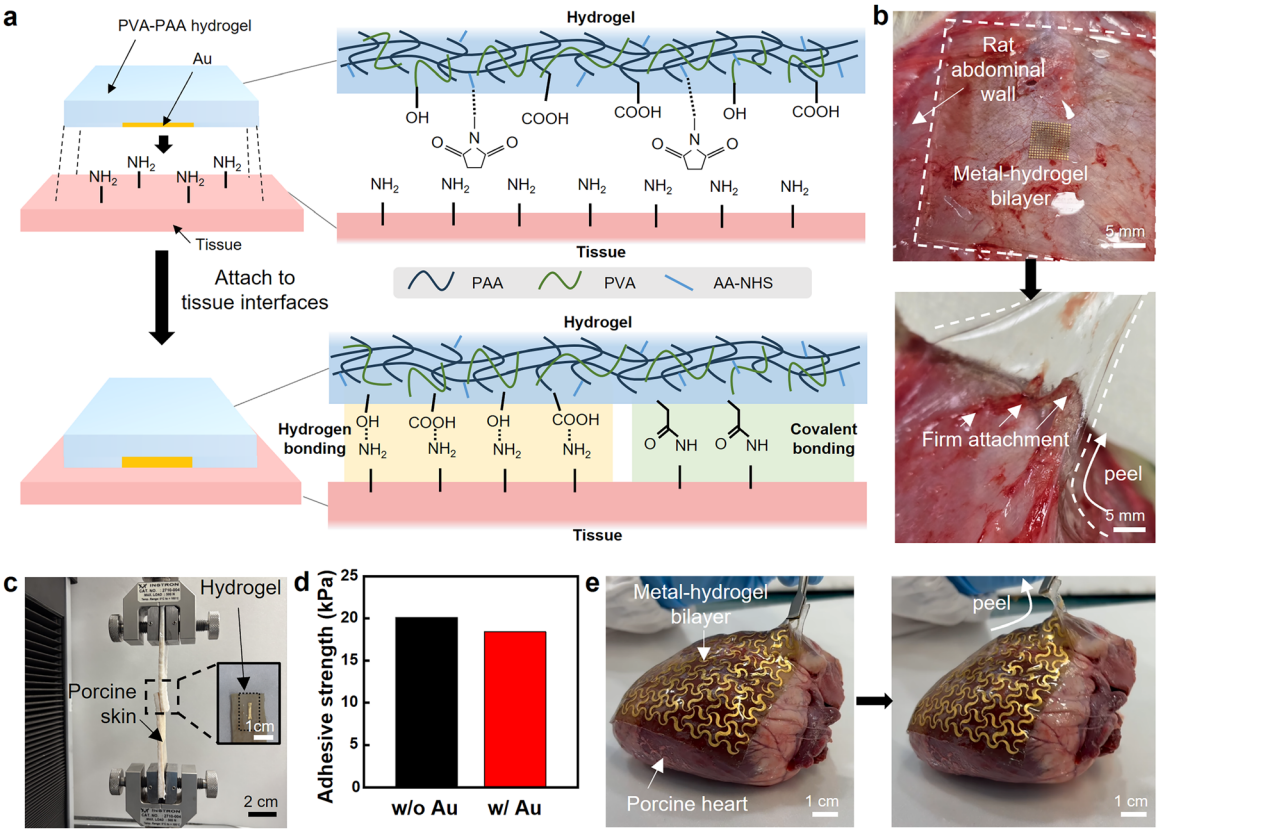

Fig. 4 Robust adhesion of the metal–hydrogel bilayer to various tissues. (a) Adhesion mechanism of the metal–hydrogel bilayer with tissue interfaces. (b) *In vivo* conformal contact and strong tissue adhesion of the metal–hydrogel bilayer on a rat abdominal wall, as demonstrated through peeling. (c) Optical photograph of the lap shear test setup. (d) Adhesive strength of the pristine hydrogel (black) and the metal–hydrogel bilayer (red) with porcine skin. (e) Optical photograph of the serpentine-mesh-patterned metal–hydrogel bilayer conformally attached to a porcine heart.

The patterned bilayer remains undamaged under external deformation (Fig. 5(g)), demonstrating its suitability for *in vivo* applications.

2.5. Epicardial applications of the bilayer

Single-pair electrode hydrogels, composed of a metal–hydrogel bilayer, were applied to the epicardial surfaces of Sprague–Dawley (SD) rats to establish electrical interfaces (Fig. 6(a)). Upon mechanical peeling, the electrodes maintained firm contact with the cardiac tissue, indicating their advantageous stability for high-fidelity signal acquisition without slippage.

Two types of hydrogel electrodes—one fabricated with the chemically anchored bilayer and the other with the physically laminated bilayer—were prepared to evaluate ligand effects. Although both hydrogel types successfully recorded epicardial electrograms from the rat heart, the chemically anchored bilayer exhibited greater signal amplitude and lower noise levels, facilitating clearer and more precise monitoring of electrophysiological signals (Fig. 6(b)). The calculated signal-to-noise ratios (SNRs) for the chemically anchored bilayer and the physically laminated bilayer electrode were 79.61 and 33.13 dB, respectively (n = 7) as supported by the *in vitro* electrochemical results (Fig. 6(c)). This improvement arises from the enhanced interfacial robustness of the chemically anchored bilayer under strain, which maintains stable charge–transfer pathways and minimizes impedance fluctuation, resulting in a higher SNR than the physically laminated counterpart.

Electrical stimulation tests were conducted to further compare the performance of the two electrode types. Both hydrogels effectively paced the heart, however, the chemically anchored bilayer demonstrated superior stimulation efficiency. As shown in Fig. 6(d), the chemically anchored bilayer captured cardiac pacing at lower energy levels (0.9 V amplitude, 1 ms duration), whereas the physically laminated bilayer required higher energy (1.2 V amplitude, 1 ms duration). The strength-duration curves (Fig. 6(e)) of the hydrogel types (n = 5, each) were also evaluated by distinguishing between capture and non-captured responses. As captured stimulation occurs when the applied voltage exceeds the tissue activation threshold, whereas non-capture appears below this level, the chemically anchored bilayer appears to pace the heart more efficiently at lower stimulation energy. Various ventricular abnormality models were implemented to highlight the practical applicability of the bilayer. First, ventricular bradycardia was induced by intraperitoneal administration of diltiazem (20 mg kg^{-1})

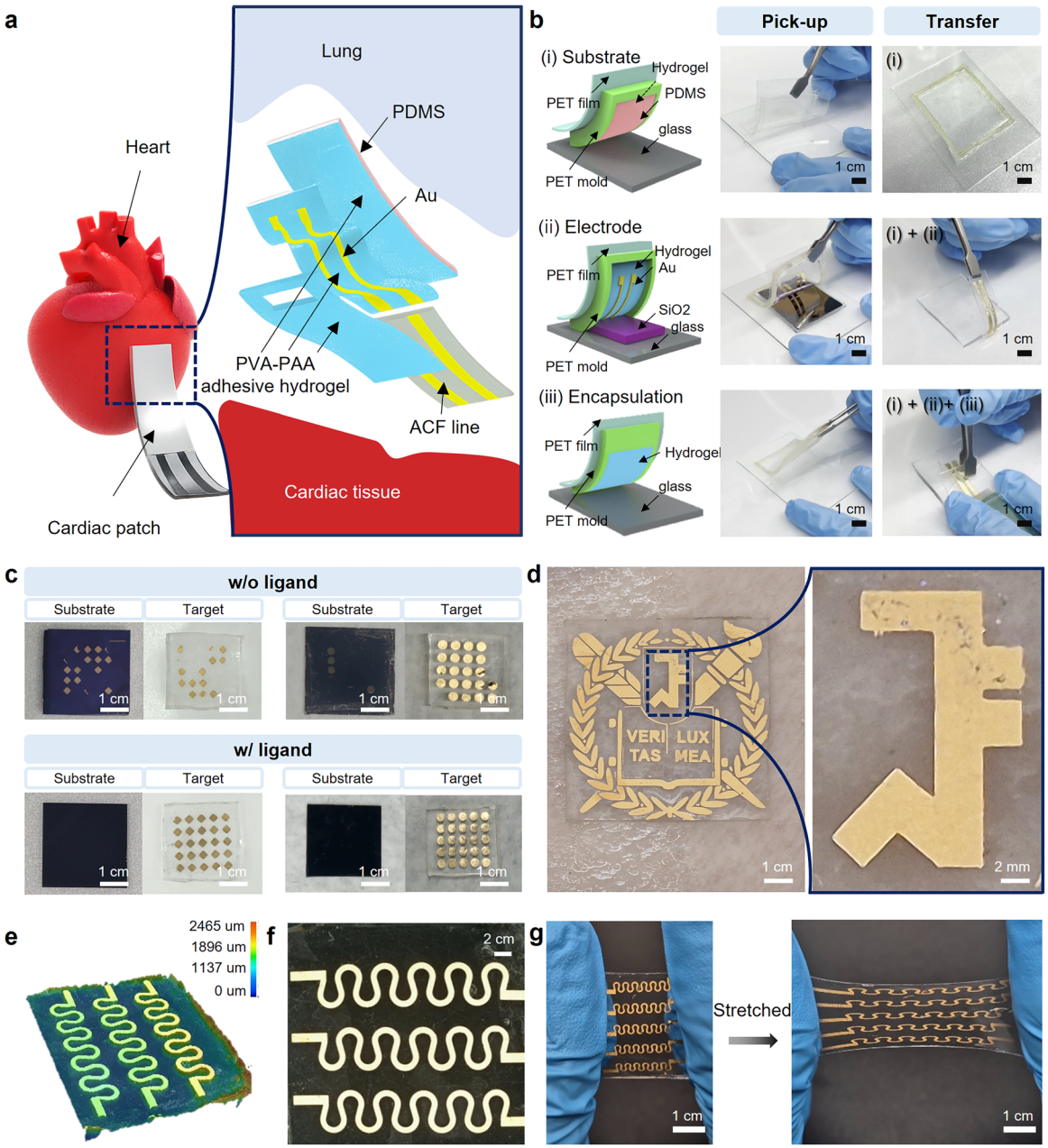

Fig. 5 Pattern versatility and practical integration of the metal–hydrogel bilayer for a stretchable cardiac interface. (a) Schematic illustration of the cardiac patch and its zoomed-in view. (b) Structural composition of each layer and the layer-by-layer assembly process to fabricate a cardiac patch. (c) Optical images of metal transfer results obtained with and without ligand treatment. "Substrate" represents the donor substrate before transfer, and "Target" represents the receiving hydrogel. Without ligand treatment (top), incomplete or uneven metal transfer is observed, whereas with ligand treatment (bottom), uniform and complete metal transfer is achieved across the patterned area. (d) Optical photographs of the patterned metal–hydrogel bilayer laminated onto porcine skin with a magnified view. (e) and (f) 3D optical images of the serpentine-patterned metal–hydrogel bilayer. (g) Optical photographs of the metal–hydrogel bilayer under uniaxial stretching.

to exhibit the ventricular activity monitoring (Fig. 7(a)). The bilayer successfully recorded delayed ventricular activity following diltiazem injection; the sinus rhythm RR interval increased from 246 to 502 ms after injection. Subsequent administration of norepinephrine (0.5 mg kg^{-1}) reduced the RR interval to 305 ms, indicating that faster ventricular rhythms were restored (Fig. 7(b)). The hydrogel bilayer effectively monitored abnormal ventricular activity, including ventricular tachyarrhythmia and premature ventricular contractions (Fig. 7(c)). As illustrated in Fig. 7(d), paired premature ventricular contractions followed by a rhythm pause were recorded over a 4 s interval when norepinephrine was administered to healthy hearts.

Electrical stimulation *via* hydrogel electrodes successfully terminated the ventricular abnormalities (Fig. 7(e)). Sustained ventricular arrhythmia was induced through myocardial

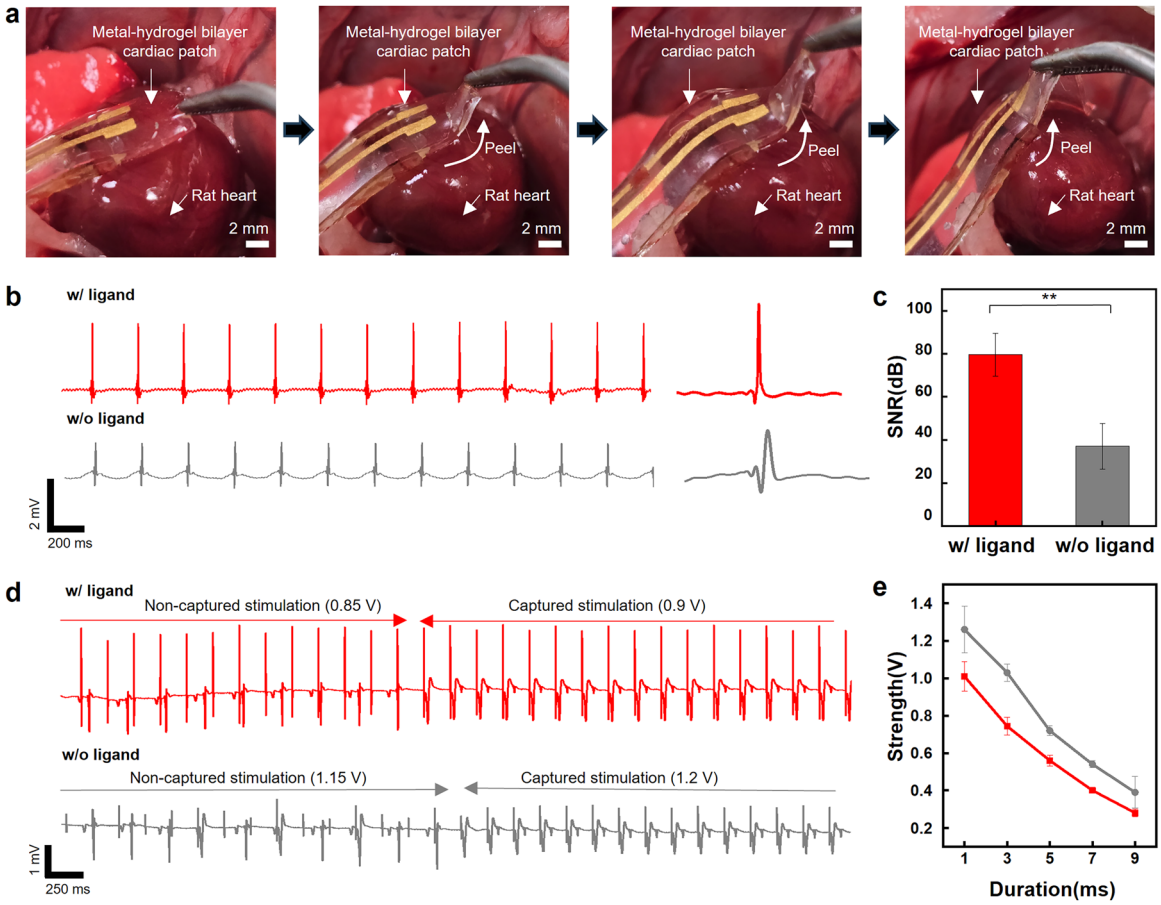

Fig. 6 Application of the metal–hydrogel bilayer patch to cardiac tissue. (a) Optical photographs showing attachment and adhesion of the metal–hydrogel bilayer cardiac patch on the epicardial surfaces. (b) Epicardial electrogram monitored using a metal–hydrogel bilayer cardiac patch with a chemically anchored bilayer (red) and a physically laminated bilayer (grey). (c) SNR of the epicardial electrogram (n = 7). (d) Surface electrocardiogram during elevating electric stimulation using an epicardial patch with a chemically anchored bilayer (red) and a physically laminated bilayer (grey). (e) Strength–duration curve of the epicardial patch with a chemically anchored bilayer (red) and a physically laminated bilayer (grey) (n = 5).

infarction and norepinephrine administration and progressed from ventricular tachyarrhythmia to ventricular fibrillation (Fig. 7(f)). After monitoring ventricular abnormalities, the therapeutic stimulation was delivered. The delivery of a high-energy electrical pulse (20 V, 10 ms) to the epicardium *via* the hydrogel electrodes effectively restored normal ventricular rhythm. Collectively, these findings demonstrate the potential of hydrogel electrodes as safe and effective epicardial bioelectronics for advanced cardiac health management.

3. Conclusions

In this study, we developed a chemically conjugated bilayer composed of a thin metal film and a soft, adhesive hydrogel. In contrast to conventional biointerfaces, this bilayer enables direct contact between the metal and biological tissue while minimizing mechanical mismatch. Covalent bonding between the metal and hydrogel forms a monolithic bilayer structure that preserves excellent electrical and electrochemical properties of the metal, even under mechanical strain. In addition, the bilayer architecture exhibits outstanding mechanical softness and strong tissue adhesiveness attributed to hydrogel.

Building upon these advantages, several considerations remain to enhance the practical potential of this platform. Although the present electrochemical characteristics align with those of conventional Au thin films, further improvements will be necessary to elevate performance—for example, through surface modification or by coating a thin layer of conductive polymer. In addition, while the present work primarily focuses on demonstrating the metal–hydrogel interfacial bonding for bioelectronic applications, the material selection of functional hydrogels and biocompatible metals should be broadened in future studies for practicality. Moreover, integrating this bilayer platform with wireless communication or power modules could open opportunities for chronic biosignal monitoring. Preclinical studies of the bilayer platform should be conducted on various organ models of large animals to analyze the safety and performance for clinical translation. Despite such requirement for clinical translation, this study provides a fundamental step

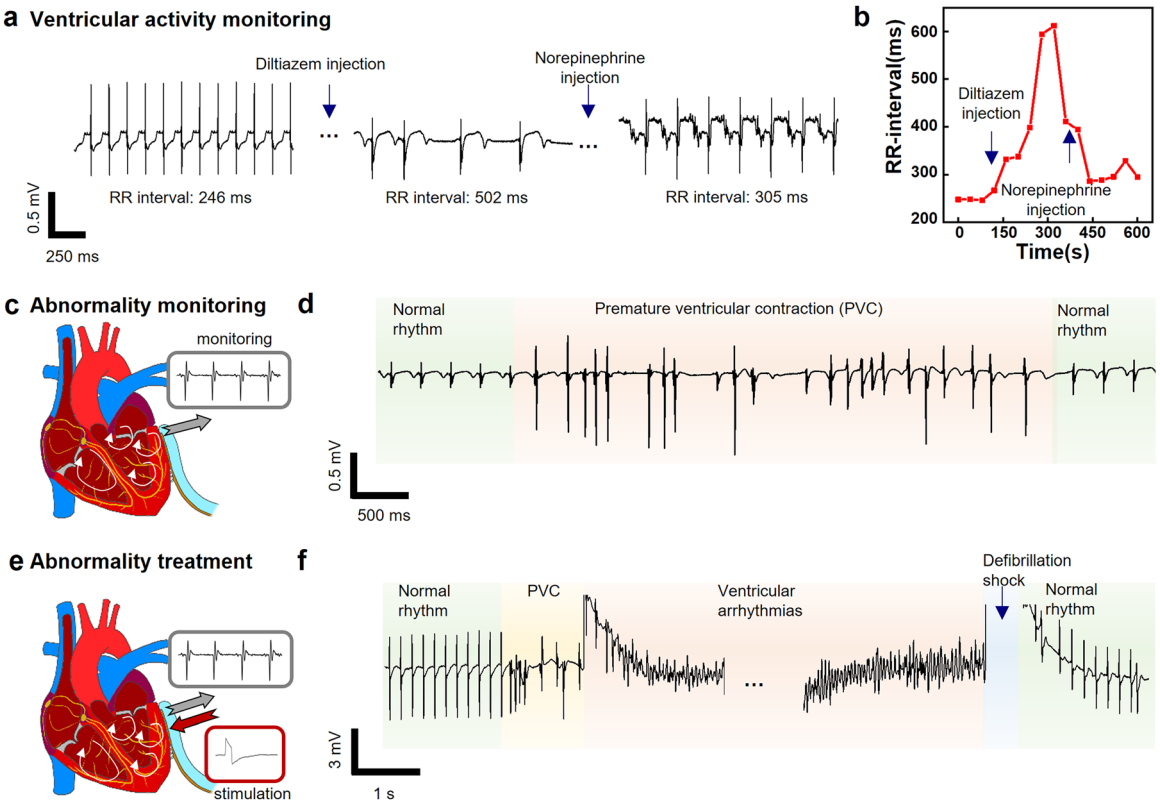

Fig. 7 Biomedical application of the metal–hydrogel patch. (a) Epicardial electrogram recorded during heartbeat modulation using drugs (diltiazem and norepinephrine). (b) Calculated RR interval during ventricular activity monitoring. (c) Schematic illustration showing epicardial signal recording on the abnormally beating heart. (d) Epicardial electrogram recorded during premature ventricular contraction. (e) Schematic illustration showing epicardial signal recording and electric stimulation on the abnormally beating heart. (f) Epicardial electrogram recorded during ventricular arrhythmias and therapeutical stimulations.

toward the metal–hydrogel bilayer electrode as a soft, tissue-conformal electronic interface for next-generation bioelectronics.

4. Experimental section

4.1. Materials

Acrylic acid, poly(vinyl alcohol) (PVA; M_w = 89 000–98 000, 99+% hydrolyzed), poly(ethylene glycol)dimethacrylate (PEGDMA), α-ketoglutaric acid, and (3-aminopropyl)triethoxysilane (APTES) were purchased form Sigma Aldrich (Germany). AA–NHS and 6-amino-1-hexanethiol hydrochloride were bought form Alfa Chemical (China). Acetone and isopropyl alcohol were obtained from Samchun Chemical (Korea). The base and curing agent of polydimethylsiloxane (PDMS; Sylgard 184) and Ecoflex 00-30 were each purchased from Dow Corning (USA) and Smooth-On (USA).

4.2. Fabrication of the PVA–PAA hydrogel

The PVA–PAA hydrogel was prepared using a previously reported method.[41] First, a hydrogel precursor solution was prepared by dissolving 35 wt% of acrylic acid, and 7 wt% of PVA in deionized water and mixing the solution at 70 °C. After mixing vigorously, the solution was cooled to room temperature (~25 °C). Then, 0.5 wt% of PEGDMA and 0.4 wt% of α-ketoglutaric acid were added to the solution. For chemical integration with the ligands and adhesion to the tissue interface, 1 wt% of AA–NHS ester was also added. The hydrogel precursor solution was poured into a mold and polymerized under ultraviolet irradiation (Fusion Cure System, Minuta Technology, Republic of Korea).

4.3. Surface functionalization of the Au film

For chemical integration between the Au film and hydrogel matrix, 6-amino-1-hexanethiol hydrochloride was grafted onto the Au layer. First, a 60 nm-thick layer of Au was deposited on a SiO_2 wafer *via* thermal evaporation. After deposition, the Au film was treated with UV/ozone for surface cleaning. Subsequently, the sample was immersed in a 10 mM of 6-amino-1-hexanethiol solution and incubated at 4 °C for 48 h. After surface treatment, the ligand-grafted Au film was rinsed to remove unbound ligand molecules.

4.4. Surface characterization

Chemical bonds between the ligand-grafted Au film and PVA–PAA hydrogel were analyzed using an FT-IR spectrometer (TENSOR27, Bruker, USA) and XPS spectrometer (Axis Supra,

Kratos, UK) installed at the National Instrumentation Center for Inter-university Research Facilities (NCIRF) at Seoul National University. Scanning electronic microscopy with energy dispersive X-ray spectroscopy (SEM-EDS) was performed to identify the surface morphology of the monolithic bilayer structure. The analysis was conducted using SEM-EDS (Auriga, Carl Zeiss, Germany) installed at the National Instrumentation Center for Environmental Management (NICEM) at the Seoul National University.

4.5. Electrical characterization

The electrical properties of the samples were measured using a Keithley Source Meter. The electrical stretchability was evaluated by applying a uniaxial strain at a rate of 0.18 mm s^{-1}. The sample (60 nm-thick Au film) had a length and width of 10 and 2 mm, respectively, and was transferred onto a 1 mm-thick hydrogel.

4.6. Fabrication of the long-term stability test device

First, the glass substrate (76 mm × 52 mm) was sequentially sonicated in acetone and isopropyl alcohol for 15 min each and dried with nitrogen. After cleaning, a 3 mm-thick PET mold matching the outer dimensions of the glass substrate was attached to surround its perimeter. The glass substrate was then spray-coated with a mold-releasing agent and dried for 10 min under ambient air. To define the central cavity for the metal–hydrogel bilayer, a 1 cm × 3 cm × 400 μm PET film was placed at the center of the mold. Next, Ecoflex 00-30 was prepared by mixing the base and curing agent in a 1 : 1 ratio, poured into the mold, and cured to form the elastomeric encapsulation layer. The cured Ecoflex was cleaned with methanol, dried with N_2, and functionalized by immersion with a 10 wt% benzophenone solution in ethanol for 30 min. After methanol rinsing and N_2 drying, a thin PVA–PAA hydrogel layer was applied in the cavity and UV-cured under ultraviolet irradiation (Fusion Cure System, Minuta Technology, Republic of Korea) for 15 min. The pre-fabricated metal–hydrogel bilayer (1 cm × 3 cm × 400 μm) was aligned with the cavity region of the elastomer–hydrogel layer and attached, and both ends of the Au electrode were connected using copper tape (3 mm × 15 cm) and silver paste.

4.7. Device setup for *in vitro* long-term stability measurement

A 9 cm × 7 cm piece of porcine skin was placed at the center of a 125 mm × 125 mm dish to serve as the tissue substrate. The fabricated device was positioned on the skin surface, and PBS solution was added until the skin was half submerged, mimicking a moist physiological environment. The copper tape at both ends of the device were connected to the probes of a B1500A semiconductor device analyzer (Agilent Technologies, USA) using alligator clips to ensure stable electrical contact. Time-dependent current profile was recorded for seven consecutive days to monitor the change in resistance over time and evaluate the long-term electrical stability of the metal–hydrogel bilayer.

4.8. Electrochemical characterization

Electrochemical measurements were performed using an electrochemical workstation (CHI660E, CH Instruments, USA). The samples were prepared with 1 cm × 1 cm Au film, using PBS as the electrolyte, Ag/AgCl as the reference electrode and Pt as the counter electrode. Electrochemical impedance spectroscopy was measured in the frequency range from 10^0 Hz to 10^6 Hz. For the charge injection capacity analysis, biphasic voltage pulses with an amplitude of ±0.5 V were applied.

4.9. Mechanical characterization

The interfacial toughness of the metal–hydrogel bilayer was measured by performing the standard 90-degree peeling test (ASTM D 2861) using a mechanical testing machine (ESM301, Mark-1, USA). Cr/Au layers were deposited on a slide glass, and the surface was functionalized with 6-amino-1-hexanethiol. Subsequently, the PVA–PAA hydrogel was cured directly on the substrate (2.5 cm × 7.5 cm). A polyethylene terephthalate (PET) film was used as the backing film and treated with APTES. This stiff PET backing, film was chemically anchored to the reverse surface of the PVA–PAA hydrogel, to prevent deformation during the peeling process. The peeling test was conducted at a peeling rate of 50 mm min^{-1}.

Tensile tests were used to measure the mechanical properties of the bilayer. The samples were prepared with length, width and thickness of 30, 20, and 0.3 mm, respectively. A universal testing machine (34SC-1, Instron) was used at a rate of 5 mm min^{-1}. The modulus of each sample was calculated within a 10% strain range. The fracture energy was calculated by comparing the results with those of the notched sample (notch length of approximately 1 cm). The displacement (mm) of the fracture point was recorded and the fracture energy (Γ) was calculated by integrating the stress-displacement curve of the unnotched sample (from zero to the fracture point) and then dividing the area by the sample width and thickness. The adhesive strength of the hydrogels was analyzed using a lap shear test (ASTM F2255) with a universal testing machine (34SC-1, Instron, USA) at a rate of 5 mm min^{-1}. The samples were prepared with an adhesion area of 2 cm × 2 cm. The maximum stress was recorded as the adhesive strength for each sample.

4.10. Fabrication of a cardiac patch

The cardiac patch was fabricated by sequentially constructing and integrating each functional layer. The PVA–PAA hydrogel served as an interfacial glue layer, enabling stable assembly of the layers.

First, the glass substrate was sequentially sonicated in acetone and isopropyl alcohol for 15 min each and dried with nitrogen. After cleaning the surface, a 200 μm-thick PET mold was attached to the glass. The glass substrate was spray-coated with a mold releasing agent and dried for 10 min under ambient air conditions. Next, the PDMS solution was prepared by blending the prepolymer and curing agent at a weight ratio of 10 : 1 and then poured onto the glass substrate. The PDMS

was blade-coated to create a uniform film. After curing, the PDMS surface was cleaned with methanol and deionized water and then functionalized by incubation in 10 wt% benzophenone solution in ethanol for 30 min. The benzophenone-treated PDMS was then rinsed with methanol and dried.

Subsequently, an adhesive hydrogel layer was prepared by attaching an additional 200 μm-thick PET mold to the top of the PDMS substrate. The PVA–PAA hydrogel precursor solution was evenly distributed and covered with the PET film. The samples were then cured under ultraviolet irradiation (Fusion Cure System, Minuta Technology, Republic of Korea) for 30 min. After exposure, a robust PDMS/hydrogel bilayer was obtained, which served as the device substrate. Next, a 60 nm-thick Au layer was transferred onto the PVA–PAA hydrogel by ligand-mediated transfer printing, as described previously. This layer was then assembled on a PDMS/hydrogel soft substrate to form a soft conductive interface. Reliable electrical interfacing was ensured by aligning an ACF and bonding it to the Au pads using heat-assisted pressing, to create robust external connections. For encapsulation and tissue interfacing 200 μm-thick PET film was laser-cut to define selective openings to the Au electrode regions. The mold was fixed onto a glass substrate, and the hydrogel precursor solution was poured into the mold and cured under ultraviolet irradiation 15 min. Finally, the encapsulating layer was aligned and attached to PDMS/hydrogel/hydrogel/Au/ACF stacks, to form a fully integrated cardiac patch.

4.11. Animal preparation for epicardial experiments

Eight-week-old male SD rats were acquired from Orient Bio Inc. (Republic of Korea). The animals underwent intratracheal intubation using an 18G intravenous catheter and were subsequently connected to a small animal ventilator (RoVent Jr., Kent Scientific, CT, USA) integrated with an isoflurane anesthetic system. Following stable anesthesia, the upper abdomen tissue immediately below the diaphragm was incised transversely to access the abdominal cavity. The thoracic cavity was exposed by incising the diaphragm *via* the abdominal route. After removing the pericardium, an epicardial patch was positioned on the left ventricular region of the heart.

4.12. Pathological monitoring and management

After animal preparation, myocardial infarction, ventricular bradycardia, and ventricular tachyarrhythmia were induced as described below. Myocardial infarction was induced by ligation of the coronary artery using a 7–0 Black Silk Suture (AILEE, Republic of Korea). Cardiac electrograms were recorded continuously before and after ligation using a data acquisition system (PowerLab, AD Instruments, New Zealand) connected to the epicardial patch. Ventricular bradycardia was induced by intraperitoneal administration of diltiazem (20 mg kg^{-1}). Subsequently ventricular pacing was performed using the same data acquisition device. Ventricular tachyarrhythmia was induced by intraperitoneal administration of high dose norepinephrine (0.5 mg kg^{-1}). Upon establishing sustained tachyarrhythmia (lasting over 30 seconds), a high-energy electrical pulse (20 V, 10 ms duration) was delivered through the epicardial patch. Electrograms were recorded and analyzed using commercial software (Lab Chart 8, AD Instruments, New Zealand).

4.13. Statistical analysis

Experimental measurements were conducted using independent samples, with the sample size (n) specified in the corresponding figure legends. In the statistical analysis for the comparison between two data groups, a two-sample t-test was performed using Excel. Statistical significance was evaluated using the following criteria: ns ($p > 0.05$), *($p \leq 0.05$), **($p \leq 0.01$), ***($p \leq 0.001$).

Ethical approval

All animal experiments were performed with approval from Seoul National University IACUC (SNU-221026-2-3). The primary aim of this animal study was to evaluate the technical feasibility and performance of the implantable materials and devices, rather than exploring biological mechanisms or therapeutic effects. Therefore, some methodological details recommended by the ARRIVE 2.0 guidelines, particularly those related to randomization, blinding, and detailed biological endpoint analyses, were not fully applicable or implemented in this work.

Author contributions

Y. A Lee, and J. Y. Lee contributed equally to this work. Y. A Lee: conceptualization, methodology, investigation, writing – original draft, writing – original draft, writing – review & editing, visualization, J. Y. Lee: conceptualization, methodology, investigation, writing – original draft, writing – original draft, writing – review & editing, visualization, J. Kim: investigation, H. Lee: investigation, S. Park: investigation, S.-H. Sunwoo: project administration, supervision, investigation (animal experiment), writing – original draft, writing – review & editing, validation, G. D. Cha: project administration, supervision, writing – original draft, writing – review & editing, validation, D.-H. Kim: project administration, supervision, writing – review & editing, validation.

Conflicts of interest

The authors declare no conflicts of interest.

Data availability

All data supporting this study are included in this article.

The data supporting this article have been included as part of the supplementary information (SI). Supplementary information is available. See DOI: https://doi.org/10.1039/d5nh00540j.

Acknowledgements

This work is supported by the Institute for Basic Science (IBS-R006-A1), the NAVER Digital Bio Innovation Research Fund, funded by NAVER Corporation (Grant No. [37-2023-0040]), and the National Research Foundation of Korea (NRF) grant funded by the Korean government (MSIT) (RS-2025-00555824 and RS-2024-00405381).

References

1 D.-H. Kim, N. Lu, R. Ma, Y.-S. Kim, R.-H. Kim, S. Wang, J. Wu, S. Won, H. Tao, A. Islam, K. J. Yu, T. Kim, R. H. Chowdhury, M. Ying, L. Xu, M. Li, H. Chung, H. Keum, M. McCormick, P. Liu, Y.-W. Zhang, F. Omenetto, Y. Huang, T. P. Coleman and J. Rogers, *Science*, 2011, **333**, 838–843.
2 Z. Liu, X. Hu, R. Bo, Y. Yang, X. Cheng, W. Pang, Q. Liu, Y. Wang, S. Wang, S. Xu, Z. Shen and Y. Zhang, *Science*, 2024, **384**, 987–994.
3 Y. Jiang, S. Ji, J. Sun, J. Huang, Y. Li, G. Zou, T. Salim, C. Wang, W. Li, H. Jin, J. Xu, S. Wang, T. Lei, X. Yan, W. Y. X. Peh, S.-C. Yen, Z. Liu, M. Yu, H. Zhao, Z. Lu, G. Li, H. Gao, Z. Liu, Z. Bao and X. Chen, *Nature*, 2023, **614**, 456–462.
4 J. Shi, Y. Dai, Y. Cheng, S. Xie, G. Li, Y. Liu, J. Wang, R. Zhang, N. Bai, M. Cai, Y. Zhang, Y. Zhan, Z. Zhang, C. Yu and C. F. Guo, *Sci. Adv.*, 2023, **9**, eadf8831.
5 S. Lee, S. Franklin, F. A. Hassani, T. Yokota, M. O. G. Nayeem, Y. Wang, R. Leib, G. Cheng, D. W. Franklin and T. Someya, *Science*, 2020, **370**, 966–970.
6 D. Jung, C. Lim, H. J. Shim, Y. Kim, C. Park, J. Jung, S. I. Han, S.-H. Sunwoo, K. W. Cho, G. D. Cha, D. C. Kim, J. H. Koo, J. H. Kim, T. Hyeon and D.-H. Kim, *Science*, 2021, **373**, 1022–1026.
7 Y. Zhao, B. Wang, J. Tan, H. Yin, R. Huang, J. Zhu, S. Lin, Y. Zhou, D. Jelinek, Z. Sun, K. Youssef, L. Voisin, A. Horrillo, K. Zhang, B. M. Wu, H. A. Coller, D. C. Lu, Q. Pei and S. Emaminejad, *Science*, 2022, **378**, 1222–1227.
8 D.-H. Kim, J. Viventi, J. J. Amsden, J. Xiao, L. Vigeland, Y.-S. Kim, J. A. Blanco, B. Panilaitis, E. S. Frechette, D. Contreras, D. L. Kaplan, F. G. Omenetto, Y. Huang, K.-C. Hwang, M. R. Zakin, B. Litt and J. A. Rogers, *Nat. Mater.*, 2010, **9**, 511–517.
9 I. R. Minev, P. Musienko, A. Hirsch, Q. Barraud, N. Wenger, E. M. Moraud, J. Gandar, M. Capogrosso, T. Milekovic, L. Asboth, R. F. Torres, N. Vachicouras, Q. Liu, N. Pavlova, S. Duis, A. Larmagnac, J. Vörös, S. Micera, Z. Suo, G. Courtine and S. P. Lacour, *Science*, 2015, **347**, 159–163.
10 J. M. Anderson, *Annu. Rev. Mater. Res.*, 2001, **31**, 81–110.
11 J. H. Koo, J.-K. Song, D.-H. Kim and D. Son, *ACS Mater. Lett.*, 2021, **3**, 1528–1540.
12 H. J. Kim, S.-H. Sunwoo, J. H. Koo and D.-H. Kim, *Korean J. Chem. Eng.*, 2025, **42**, 2037–2068.
13 S. I. Han, S.-H. Sunwoo, C. S. Park, S.-P. Lee, T. Hyeon and D.-H. Kim, *ACS Nano*, 2024, **18**, 12025–12048.
14 B. Zhu, S. Gong and W. Cheng, *Chem. Soc. Rev.*, 2019, **48**, 1668–1711.
15 C. F. Guo, T. Sun, Q. Liu, Z. Suo and Z. Ren, *Nat. Commun.*, 2014, **5**, 3121.
16 K.-I. Jang, H. U. Chung, S. Xu, C. H. Lee, H. Luan, J. Jeong, H. Cheng, G.-T. Kim, S. Y. Han, J. W. Lee, J. Kim, M. Cho, F. Miao, Y. Yang, H. N. Jung, M. Flavin, H. Liu, G. W. Kong, K. J. Yu, S. I. Rhee, J. Chung, B. Kim, J. W. Kwak, M. H. Yun, J. Y. Kim, Y. M. Song, U. Paik, Y. Zhang, Y. Huang and J. A. Rogers, *Nat. Commun.*, 2015, **6**, 6566.
17 J. Rogers, T. Someya and Y. Huang, *Science*, 2010, **327**, 1603–1607.
18 S. Choi, S. I. Han, D. Jung, H. J. Hwang, C. Lim, S. Bae, O. K. Park, C. M. Tschabrunn, M. Lee, S. Y. Bae, J. W. Yu, J. H. Ryu, S.-W. Lee, K. Park, P. M. Kang, W. B. Lee, R. Nezafat, T. Hyeon and D.-H. Kim, *Nat. Nanotechnol.*, 2018, **13**, 1048–1056.
19 J. Park, S. Choi, A. H. Janardhan, S.-Y. Lee, S. Raut, J. Soares, K. Shin, S. Yang, C. Lee, K.-W. Kang, H. R. Cho, S. J. Kim, P. Seo, W. Hyun, S. Jung, H.-J. Lee, N. Lee, S. H. Choi, M. Sacks, N. Lu, M. E. Josephson, T. Hyeon, D.-H. Kim and H. J. Hwang, *Sci. Transl. Med.*, 2016, **8**, 344ra86–344ra86.
20 H. Joo, D. Jung, S.-H. Sunwoo, J. H. Koo and D.-H. Kim, *Small*, 2020, **16**, e1906270.
21 Y. Xu, Z. Ye, G. Zhao, Q. Fei, Z. Chen, J. Li, M. Yang, Y. Ren, B. Berigan, Y. Ling, X. Qian, L. Shi, I. Ozden, J. Xie, W. Gao, P.-Y. Chen and Z. Yan, *Nat. Nanotechnol.*, 2024, **19**, 1158–1167.
22 T. Dvir, B. P. Timko, M. D. Brigham, S. R. Naik, S. S. Karajanagi, O. Levy, H. Jin, K. K. Parker, R. Langer and D. S. Kohane, *Nat. Nanotechnol.*, 2011, **6**, 720–725.
23 J. Kim, G. D. Cha, M. Kim, S.-P. Lee, S.-H. Sunwoo and D.-H. Kim, *Adv. Nanobiomed Res.*, 2025, **5**, 2400143.
24 N. Bowden, S. Brittain, A. G. Evans, J. W. Hutchinson and G. M. Whitesides, *Nature*, 1998, **393**, 146–149.
25 Z. Jiang, N. Chen, Z. Yi, J. Zhong, F. Zhang, S. Ji, R. Liao, Y. Wang, H. Li, Z. Liu, Y. Wang, T. Yokota, X. Liu, K. Fukuda, X. Chen and T. Someya, *Nat. Electron.*, 2022, **5**, 784–793.
26 S. Chae, W. J. Choi, L. J. Nebel, C. H. Cho, Q. A. Besford, A. Knapp, P. Makushko, Y. Zabila, O. Pylypovskyi, M. W. Jeong, S. Avdoshenko, O. Sander, D. Makarov, Y. J. Chung, A. Fery, J. Y. Oh and T. I. Lee, *Nat. Commun.*, 2024, **15**, 3071.
27 Y. Shin, S. Hong, Y. C. Hur, C. Lim, K. Do, J. H. Kim, D.-H. Kim and S. Lee, *Nat. Mater.*, 2024, **23**, 1411–1420.
28 H. Shim, K. Sim, B. Wang, Y. Zhang, S. Patel, S. Jang, T. J. Marks, A. Facchetti and C. Yu, *Nat. Electron.*, 2023, **6**, 349–359.
29 J. H. Koo, J. Kang, S. Lee, J.-K. Song, J. Choi, J. Yoon, H. J. Park, S.-H. Sunwoo, D. C. Kim, W. Nam, D.-H. Kim, S. G. Im and D. Son, *Nat. Electron.*, 2023, **6**, 137–145.
30 D. Zhong, C. Wu, Y. Jiang, Y. Yuan, M.-G. Kim, Y. Nishio, C.-C. Shih, W. Wang, J.-C. Lai, X. Ji, T. Z. Gao, Y.-X. Wang, C. Xu, Y. Zheng, Z. Yu, H. Gong, N. Matsuhisa, C. Zhao, Y. Lei, D. Liu, S. Zhang, Y. Ochiai, S. Liu, S. Wei, J. B.-H. Tok and Z. Bao, *Nature*, 2024, **627**, 313–320.
31 S. Wang, J. Xu, W. Wang, G. Wang, R. Rastak, F. Molina-Lopez, J. W. Chung, S. Niu, V. Feig, J. Lopez, T. Lei, S. Kwon,

Y. Kim, A. Foudeh, A. Ehrlich, A. Gasperini, Y. Yun, B. Murmann, J. B.-H. Tok and Z. Bao, *Nature*, 2018, **555**, 83–88.
32 W. Wang, S. Wang, R. Rastak, Y. Ochiai, S. Niu, Y. Jiang, P. K. Arunachala, Y. Zheng, J. Xu, N. Matsuhisa, X. Yan, S.-K. Kwon, M. Miyakawa, Z. Zhang, R. Ning, A. M. Foudeh, Y. Yun, C. Linder, J. B.-H. Tok and Z. Bao, *Nat. Electron.*, 2021, **4**, 143–150.
33 K. W. Cho, S.-H. Sunwoo, Y. J. Hong, J. H. Koo, J. H. Kim, S. Baik, T. Hyeon and D.-H. Kim, *Chem. Rev.*, 2022, **122**, 5068–5143.
34 H. Yuk, T. Zhang, S. Lin, G. A. Parada and X. Zhao, *Nat. Mater.*, 2016, **15**, 190–196.
35 Z. Pan, Q.-Q. Fu, M.-H. Wang, H.-L. Gao, L. Dong, P. Zhou, D.-D. Cheng, Y. Chen, D.-H. Zou, J.-C. He, X. Feng and S.-H. Yu, *Nat. Commun.*, 2023, **14**, 5378.
36 Y. Shin, H. S. Lee, Y. J. Hong, S.-H. Sunwoo, O. K. Park, S. H. Choi, D.-H. Kim and S. Lee, *Sci. Adv.*, 2024, **10**, eadi7724.
37 J. Yi, G. Zou, J. Huang, X. Ren, Q. Tian, Q. Yu, P. Wang, Y. Yuan, W. Tang, C. Wang, L. Liang, Z. Cao, Y. Li, M. Yu, Y. Jiang, F. Zhang, X. Yang, W. Li, X. Wang, Y. Luo, X. J. Loh, G. Li, B. Hu, Z. Liu, H. Gao and X. Chen, *Nature*, 2023, **624**, 295–302.
38 C. Lim, S. Lee, H. Kang, Y. S. Cho, D.-H. Yeom, S.-H. Sunwoo, C. Park, S. Nam, J. H. Kim, S.-P. Lee, D.-H. Kim and T. Hyeon, *Adv. Mater.*, 2024, **36**, e2407931.
39 Y. Kim, J. Zhu, B. Yeom, M. Di Prima, X. Su, J.-G. Kim, S. J. Yoo, C. Uher and N. A. Kotov, *Nature*, 2013, **500**, 59–63.
40 C. Lim, C. Park, S.-H. Sunwoo, Y. G. Kim, S. Lee, S. I. Han, D. Kim, J. H. Kim, D.-H. Kim and T. Hyeon, *ACS Nano*, 2022, **16**, 10431–10442.
41 C. Lim, S. Lee, H. Kang, Y. S. Cho, D.-H. Yeom, S.-H. Sunwoo, C. Park, S. Nam, J. H. Kim, S.-P. Lee, D.-H. Kim and T. Hyeon, *Adv. Mater.*, 2024, **36**, e2407931.
42 D. Won, J. Kim, J. Choi, H. Kim, S. Han, I. Ha, J. Bang, K. K. Kim, Y. Lee, T.-S. Kim, J.-H. Park, C.-Y. Kim and S. H. Ko, *Sci. Adv.*, 2022, **8**, eabo3209.
43 Y. Ohm, C. Pan, M. J. Ford, X. Huang, J. Liao and C. Majidi, *Nat. Electron.*, 2021, **4**, 185–192.
44 Y. Chen, D. Estevez, Z. Zhu, Y. Wang, Y.-W. Mai and F. Qin, *ACS Appl. Mater. Interfaces*, 2024, **16**, 29267–29281.
45 Y. Xue, X. Li, H. Li and W. Zhang, *Nat. Commun.*, 2014, **5**, 4348.
46 J. Wu, J. Deng, G. Theocharidis, T. L. Sarrafian, L. G. Griffiths, R. T. Bronson, A. Veves, J. Chen, H. Yuk and X. Zhao, *Nature*, 2024, **630**, 360–367.
47 Y. Ji, X. Yang, Z. Ji, L. Zhu, N. Ma, D. Chen, X. Jia, J. Tang and Y. Cao, *ACS Omega*, 2020, **5**, 8572–8578.
48 Y.-R. Xue, C. Liu, Z.-Y. Ma, C.-Y. Zhu, J. Wu, H.-Q. Liang, H.-C. Yang, C. Zhang and Z.-K. Xu, *Nat. Commun.*, 2024, **15**, 1539.
49 S. Wang, J. Song, D.-H. Kim, Y. Huang and J. A. Rogers, *Appl. Phys. Lett.*, 2008, **93**, 023126.
50 T.-H. Kim, W. M. Choi, D.-H. Kim, M. A. Meitl, E. Menard, H. Jiang, J. A. Carlisle and J. A. Rogers, *Adv. Mater.*, 2008, **20**, 2171–2176.
51 J. Deng, H. Yuk, J. Wu, C. E. Varela, X. Chen, E. T. Roche, C. F. Guo and X. Zhao, *Nat. Mater.*, 2021, **20**, 229–236.

